Journal of the Australian Ceramic Society (2025) 61:1275–1291
https://doi.org/10.1007/s41779-025-01162-7

RESEARCH

High-performance photocatalytic degradation of binary mixture of RhB and DR23 dyes under UV irradiation using nanosized-ZnO

Erman Erdogan[1] · **Mehmet Erkol**[2] · **Burcu Bozkurt Cirak**[3] · **Mehmet Yilmaz**[4,5]

Received: 27 November 2024 / Revised: 22 January 2025 / Accepted: 3 February 2025 / Published online: 21 February 2025

Abstract

Zinc oxide (ZnO) structures are used in the field of environmental issues, especially photocatalysts, due to their superior physical and chemical properties. In this study, ZnO structures were produced using the hydrothermal technique. The physical and photocatalytic properties of the synthesized ZnO structures were investigated. The crystal size of ZnO was calculated using XRD patterns and found to be 27–36 nm using the modified Scherrer equation, 33–40 nm using the Williamson Hall model depending on the precursor amount. Scanning electron microscope (SEM) images of the produced ZnO structures revealed that it had a structure in the form of cauliflower morphology. Changing of the ZnO structure with decreasing precursor amounts clearly narrowed the band gap energy. Experimental studies of photocatalytic activity of ZnO photocatalysts were examined in a UV-cabinet, under Ultraviolet–A (UVA) light irradiation and by degradation of Rhodamine B (RhB) and Direct Red 23 (DR23) binary mixture of dyestuff against time. As a result of the experimental studies, it was observed that the photocatalytic activity of ZnO structure showed 97.16% higher degradation efficiency in 180 min. In line with kinetic studies, the photocatalytic half-life of the RhB + DR23 dyestuff was calculated between 31.79 min and 52.91 min for all structures, reaction rate constant (k) was calculated as highest 0.0218 1/min for Z 36.6 RhB degradation, and the regression coefficient (R^2) values were calculated between 0.54 and 0.98 for all structures.

Keywords ZnO · Photocatalytic activity · Hydrothermal synthesis · Binary mixture · Dyestuffs · RhB and DR23

Introduction

Water is a basic resource for the survival of all living organisms. Only 0.03% of the water on the Earth's surface is suitable for human consumption. Since the late 20th century, pollution of clean water resources has become a serious problem with the development of transportation and urban drainage systems, industrial waste, human activities and agricultural activities [1, 2]. The life of living things is negatively affected by the mixing of harmful organic/inorganic substances into clean water. Inorganic substances include metal acid and heavy metal ions [3], oxyacid ions [4], pesticides [5] and organic dyes [6] cause the light penetration value range to narrow.

Rhodamine B (RhB) and Direct Red 23 (DR23) are examples of organic dyes that are widely used in various industries such as textiles, paper and food due to their water solubility and effectiveness. However, their use raises environmental safety concerns [7–10]. Therefore, purification of these polluting dye groups from clean water sources has become a scientific and technological issue. In this context,

---

✉ Erman Erdogan
erman.erdogan@bilecik.edu.tr

✉ Burcu Bozkurt Cirak
bbcirak@erzincan.edu.tr

[1] Electronic Communication Technology Program, Vocational High School, Bilecik Seyh Edebali University, Bilecik 11100, Turkey

[2] Department of Science Teaching, Education Faculty, Afyon Kocatepe University, Afyon 03200, Turkey

[3] Department of Alternative Energy Sources, Vocational High School, Erzincan University, Erzincan 24000, Turkey

[4] Department of Science Teaching, K.K. Education Faculty, Ataturk University, Erzurum 25240, Turkey

[5] Department of Science Teaching, Education Faculty, Suleyman Demirel University, Isparta 32260, Turkey

expectations from developing technologies have to meet the environmental and economic demands and at the same time offer the desired level of material functionality and efficacy. Therefore, the purification of wastewater from organic dye effluents and the increasing demand for clean water resources worldwide are widely investigated by researchers [11, 12]. Different water purification methods have been developed depending on the type and density of impurities in the water. A variety of techniques, including membranes [13], filtration [14], electrochemistry [15] and photocatalysis [16], have been employed in the physico-chemical and biological treatment process. Some of these processes are expensive and inefficient, and can produce harmful side products [17]. Therefore, environmentally friendly piezocatalysis can be given as an example. It has recently been used for the treatment of wastewater [18]. Piezoelectric catalysis takes advantage of the piezoelectric effect and uses mechanical vibration to produce active species on opposite surfaces of matter for degradation of dye. Piezoelectric materials might benefit from a built-in electric field because of their inherent non-centrosymmetric property [19].

Photocatalysis has recently attracted a great deal of research attention as a highly efficient and environmentally friendly treatment of by-products, and is seen as a promising technology with the potential to improve air and water quality, reduce energy consumption and reduce pollution [20]. The photocatalyst, activated by visible light or UV light irradiation, converts pollutants in wastewater into non-toxic, harmless inorganic products such as carbon dioxide (CO_2) and water (H_2O). In this context, studies on the development of new materials have been increased to prevent dye contamination and increase photocatalytic efficiency. Transition metals, metal nitrides, metal sulphides, perovskites, noble metals, metal oxides and carbon-based materials are classes of materials commonly used as photocatalysts [21, 22]. Metal oxides are the most ideal nanomaterials for water and wastewater treatment with their high surface-to-volume ratio and surface areas [23]. In studies, semiconductor metal oxides such as zinc oxide (ZnO) [24], iron oxide (Fe_2O_3) [25], titanium dioxide (TiO_2) [26] and tungsten oxide (WO_3) [27] attract great attention in photocatalytic applications.

Among these materials, ZnO is the most widely used photocatalyst compared to other semiconductor materials with its many superior properties. ZnO is used in dyestuffs, pharmaceutical industry, plastic materials, food, beverage and dry foods, etc [28]. It is a non-toxic semiconductor widely used as a pigment and filler for whitening. It also appears as a UV absorber, which is frequently preferred in the cosmetic industry and beauty care products. With the development of industry, nano-structured ZnO is solution-oriented for removing inorganic and organic pollutants from water, cleaning of various diseases caused by dirty water, asthma, many harmful bacteria from dirty water, having a photovoltaic mechanism to collect the energy from the sun in a certain area [29]. He et al. [30] conducted a study on the photocatalytic degradation of methyl orange dye at a concentration of 20 mg/L using ZnO photocatalysts of various characteristic structures and sizes produced by the solvothermal method. The ZnO photocatalyst with the highest photocatalytic activity resulted in the decolouration of 44% of the methyl orange dye within 20 min, which suggests that the photocatalytic activity is influenced by the characteristic structure of the photocatalyst. Chen et al. [31] conducted a study on the production of ZnO nanocrystals through solvothermal reactions of n-butylamine and tetrahydrofuran with zinc acetate. They investigated the photocatalytic performance of ZnO nanocrystals prepared by different methods in degrading methyl orange dye and found that their most efficient sample degrades 85% of methylene orange dye in 180 min. The literature suggests that nanoparticles with varying geometries display distinct characteristics and, consequently, different photocatalytic efficiencies [32]. Our study is aimed to enhance the interaction between ZnO and organic dye by utilizing the numerous nanoscale protrusions and branches of ZnO nanoparticles in the cauliflower geometry [33, 34]. Thus, the aim is to achieve efficient adsorption of organic pollutants and high absorption of incident radiation by providing high light scattering and reflection through the hierarchical structure of cauliflower geometry [35]. Currently, various methodologies have been employed for the synthesis of zinc oxide (ZnO) nanoparticles [36, 37]. Notably, the hydrothermal approach stands out as being particularly conducive to yielding ZnO nanoparticles with cauliflower morphology. This method facilitates the tailored manipulation of synthesis parameters, including reaction temperature, duration, and precursor concentration. In recent studies, ZnO nanoparticles were prepared by the hydrothermal method for dye treatment technologies overlooks piezocatalysis and photocatalysis. Thin carbon/ZnO showed superior performance in piezoelectric catalytic degradation of RhB [38]. In another study, composite catalyst prepared by modifying $ZnSnO_3$ and zeolitic imidazolate framework-8 (ZIF-8) by a simple hydrothermal method and demonstrated enhanced photocatalytic activity in CO_2 reduction [39]. The obtained $ZnSnO_3/Bi_4Ti_3O_{12}$ catalysts significantly enhanced the piezocatalytic degradation performance of RhB [40]. By subjecting zinc precursor solutions to high-temperature and high-pressure conditions in the presence of a hydroxide source, the hydrothermal method ensures effective nucleation, thereby fostering the formation of ZnO nanoparticles characterized by the desired cauliflower geometry [41].

In this study, ZnO photocatalyst structure with different precursor concentration was synthesized by hydrothermal method. With the photocatalytic effect, under UV light irradiation, the binary mixture of RhB and DR23 dyestuff was degraded and transformed into harmless products, and the degradation efficiency of the dye was calculated using the UV-vis spectrophotometer and the degradation efficiency equation of photocatalysts against time in photocatalytic processes.

Experimental

To synthesize ZnO structures, the method used for ZnO synthesis in the literature was used [42], and different amounts (36.6, 46.6 and 56.6 mM) of the precursor zinc chloride ($ZnCl_2$) were used in our study. 0.498 g, 0.635 g, and 0.771 g of these amounts were dissolved in double distilled water until the pH value was 9, using triethylamine (TEA) as a pH adjuster. The prepared solution was mixed in an ultrasonic bath for approximately 10 min until a homogeneous mixture was achieved. After the mixing process was completed, the resulting solution was rested at room temperature for 1 h and transferred to a 100 mL teflon autoclave and kept at 200 °C for 2 h. After the obtained material was cooled at room temperature, it was washed first with ethanol and then with pure water to remove impurities and left to dry at room temperature. The structures synthesized in the presence of different amounts of precursor are named Z 36.6, Z 46.6, and Z 56.6. The experimental mechanism of ZnO photocatalytic experiment on RhB + DR23 binary dye mixture is given in Fig. 1.

In this section, the structural, morphological, and photocatalytic properties of ZnO structures prepared by the hydrothermal synthesis technique were examined in detail using various analytical techniques. Structural properties of ZnO structures such as phases, half maximum peak width, crystallization levels, and grain size were examined using the X-ray diffraction technique. SEM and EDS microscopes were used to determine the morphological properties and elemental contents of ZnO structures. Finally; the photocatalytic activities of ZnO structures were investigated using the aqueous solution of RhB and DR23 binary mixture dyestuffs, which are organic impurities. To achieve this, a mixture was prepared by combining 22 ml of Rhodamine B (RhB) solution with a concentration of 5 parts per million (ppm) and 28 ml of Direct Red 23 (DR-23) dye solution with a concentration of 30 ppm. Given that the dye content of the DR-23 solution was 30%, its absorbance was adjusted to match that of the 5 ppm RhB solution. Additionally, in the photocatalytic performance tests, a catalyst mass of 40 mg was employed. Photocatalytic properties of ZnO structures, such as photocatalytic rate constant and photocatalytic efficiency, were determined.

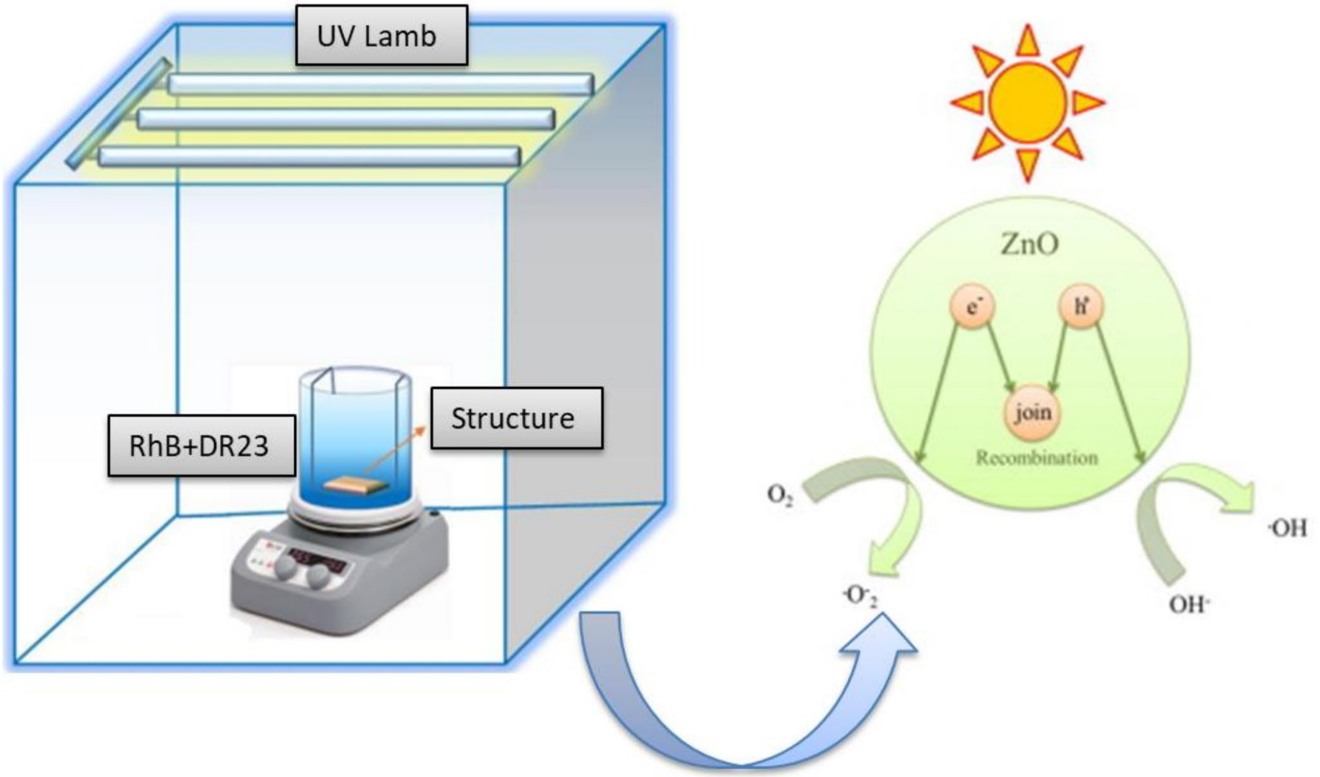

Fig. 1 The experimental mechanism of ZnO photocatalytic on RhB + DR23 binary dye mixture

Results and discussions

XRD analysis

X-ray Diffraction (XRD) analysis helps determine the crystal structure of the material, crystal size, crystallite size distribution and purity of the material. XRD was used to investigate the nature of the crystal growth and the phases in which the prepared material were formed. XRD patterns of ZnO structures with different amounts of precursors produced by the hydrothermal synthesis method were obtained at 40 kV voltages and 40 mA current using CuKα radiation with a wavelength of 0.154 nm in the range of 20–80°. Data were collected with an angular resolution of 0.02°. Our research focuses on using XRD to investigate the crystal properties of ZnO structures. Primary objectives include identifying synthesized ZnO structures and examining the effect of Zn precursor concentration on diffraction peaks. The XRD patterns to be used for this purpose are shown in Fig. 2.

Accordingly, when the XRD diffraction patterns of the produced ZnO structures were examined, it was seen that the full width half maximum (FWHM) of the obtained peaks were small and their crystallization levels were high. Surfaces with high energy are thought to lead to faster crystallization. Conversely, surfaces with low energy are found to expand slowly. This phenomenon implies that crystal planes with low surface energy are favored. In general, the most intense peaks in XRD diffractions correspond to exposed crystal surfaces with low energy [43]. The presence of 11 peaks with different intensities and widths (100), (002), (101), (102), (110), (103), (200), (112), (201), (004), and (202) indicate that the ZnO structures are produced. This is an indication that it has a polycrystalline structure. In addition, these detected peaks are characteristic diffraction peaks of ZnO. All these diffraction peaks consist of wurtzite (hexagonal) structure compatible with JCPDS Card No 36-1451 and space group P63mc [44]. Interestingly, a new phase was formed in the sample synthesized with 46.6 mM $ZnCl_2$ precursor. This phase was identified as chloride lamellar phase ($Zn_5(OH)_8Cl_2.H_2O$). Further increasing and decreasing the $ZnCl_2$ precursor concentration, only ZnO is formed and the chloride phases disappear. Here, the incomplete conversion of ZnO may be due to the agglomeration or nucleation of the chloride phases of $ZnCl_2$ at a concentration of 46.6 mM. Another possible reason for this situation is the change in the reaction kinetics between $ZnCl_2$ and [OH-] at the same concentration. It is important to note that this analysis is based solely on the experimental parameters and not on subjective assessments. Also, it has been reported that a similar phase is formed in ZnO structures using different $ZnCl_2$ precursor values [45, 46]. High concentrations of the zinc precursor can lead to an increased presence of Zn^{2+} ions during the hydrothermal process. This contributes to the formation of more Zn-O bonds in the resulting ZnO thin films and potentially affects the crystallinity of the films. Higher concentrations of Zn^{2+} can potentially promote enhanced crystal growth and larger crystal sizes, thus affecting the overall structural quality of ZnO films [47]. This suggests that the concentration of zinc precursor plays an important role in modulating the structural properties of the material during the hydrothermal process.

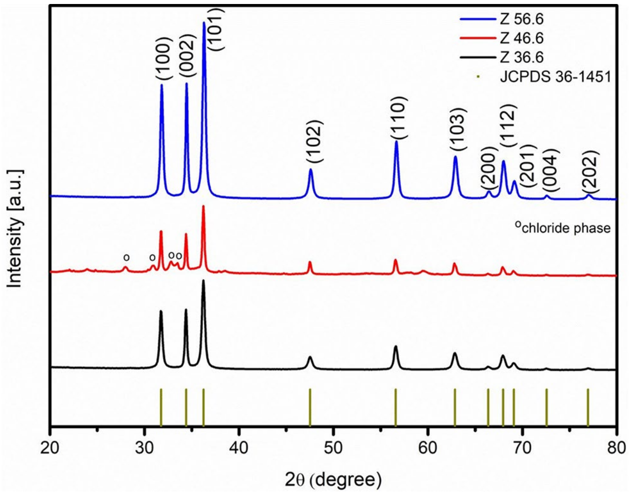

Fig. 2 X-ray diffraction pattern of ZnO structures

Crystallite size values of ZnO structures were calculated by modified Debye-Scherrer (D-R) and Williamson-Hall (W-H) methods using XRD data. Debye-Scherrer develops a correlation that gives the relationship between crystallite size (D) and peak width and is given in equation below [48]:

$$\ln\beta = ln\frac{0.9\,\lambda}{D} + ln\frac{1}{\cos\theta}$$

Here, D is the average crystallite size, λ is the X-ray wavelength, β is the half-peak width (radians) of the maximum intensity peak, and θ is the XRD diffraction angle of the maximum intensity peak. As can be seen from Fig. 3 (a), if we plot the data for lnβ to ln (1/cos θ), a slope with a line and a crossing of ln 0.9λ/D should have existed. The values calculated using this equation is given in Table 1.

According to W-H method, the crystal dimensions can be calculated by the equation shown below [49]:

$$\beta\, cos\theta = \frac{K\lambda}{D} + 4\epsilon\, sin\theta$$

When this equation is expressed according to the equation y = x + b, the y-axis indicates $\beta cos\theta$ and the x-axis indicates $4sin\theta$. Therefore, when the graph is drawn using the θ and

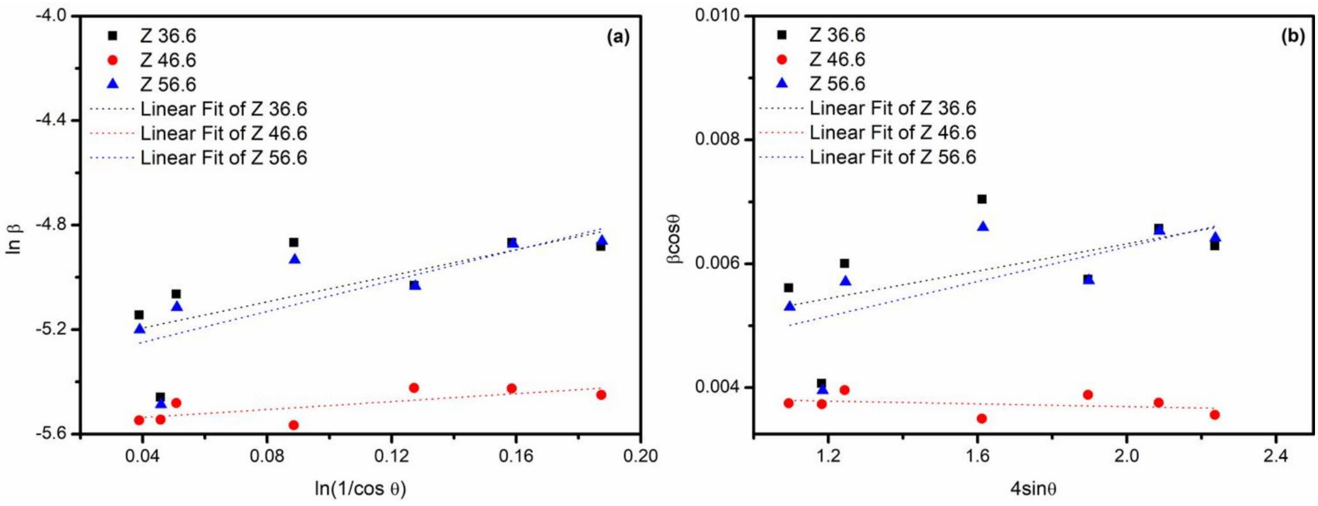

Fig. 3 Crystallite size graphs of ZnO structures by (**a**) D-R and (**b**) W-H method

Table 1 Various parameters from structural examination (d_{hkl}: interplanar distance, FWHM: full-width half maximum, D_{SR}: the size of crystal obtained from Scherrer plot, D_{WH}: the size of crystal obtained from Williamson-Hall plot

Precursor concentration	(hkl)	d_{hkl}(Å)	2θ (°)	FWHM(°)	D_{SR}(nm)	D_{WH}(nm)
36.6 mM	(100)	2.8149	31.75	0.3342	27.59	33.72
	(002)	2.6046	34.39	0.2440		
	(101)	2.4764	36.23	0.3620		
	(102)	1.9107	47.53	0.4410		
	(110)	1.6244	56.59	0.3741		
	(103)	1.4768	62.85	0.4412		
	(112)	1.3778	67.95	0.4345		
46.6 mM	(100)	2.8149	31.75	0.2233	36.26	39.94
	(002)	2.6039	34.40	0.2238		
	(101)	2.4764	36.23	0.2387		
	(102)	1.9111	47.52	0.2191		
	(110)	1.6246	56.58	0.2528		
	(103)	1.4770	62.84	0.2522		
	(112)	1.3775	67.97	0.2461		
56.6 mM	(100)	2.8089	31.82	0.3158	29.67	35.35
	(002)	2.5995	34.46	0.2373		
	(101)	2.4718	36.30	0.3442		
	(102)	1.9080	47.60	0.4125		
	(110)	1.6225	56.66	0.3729		
	(103)	1.4753	62.92	0.4384		
	(112)	1.3768	68.01	0.4436		

β values obtained according to the XRD output, the average crystal size can be calculated since its value is known from the Kλ/D part, which expresses the b value according to the equation $y = ax + b$ as illustrated in Fig. 3 (b). The values calculated using this equation is given in Table 1.

The observed change in crystal size at low concentrations followed by a more gradual change at higher concentrations can be attributed to the growth dynamics during hydrothermal synthesis [50]. At low precursor concentrations, crystal formation starts because of a preferred nucleation condition and crystal size changes because of a threshold concentration required for effective nucleation. When the precursor concentration is increased to higher values, the system jumps from a nucleation-dominated phase to a growth-dominated phase, resulting in a change in crystal size. While the interplay between precursor concentration and crystal size facilitates faster crystal growth of higher concentrations, it can also lead to increased nucleation density and challenges such as potential agglomeration [51]. In the literature survey, the average crystallite size values obtained for ZnO nanoparticles conducted by Mustapha et al., the W-H and D-R analysis showed large differences and the crystal size recorded as much higher as compared to our results [52]. The crystallite size of ZnO nanostructures with different zinc acetate dehydrate concentration conducted by Rajamanickam et al. reported that, the largest crystallite size was at 56.34 nm, while the smallest value was 42.26 nm [53].

Morphological analysis

Figure 4 shows the SEM images of the ZnO structures used in the study. The fact that semi-spherical nanoparticles appear larger in some regions is due to agglomeration. When these images are examined, the general appearance of ZnO structures using different precursor concentrations shows that they have morphology called “cauliflower”. ZnO is a polar crystal with a basal positive polar plane (0001) and a negative polar plane (000–1) [54]. The positive polar plane is rich in Zn, while the negative polar plane is rich in O. These polar planes are thermodynamically unstable due

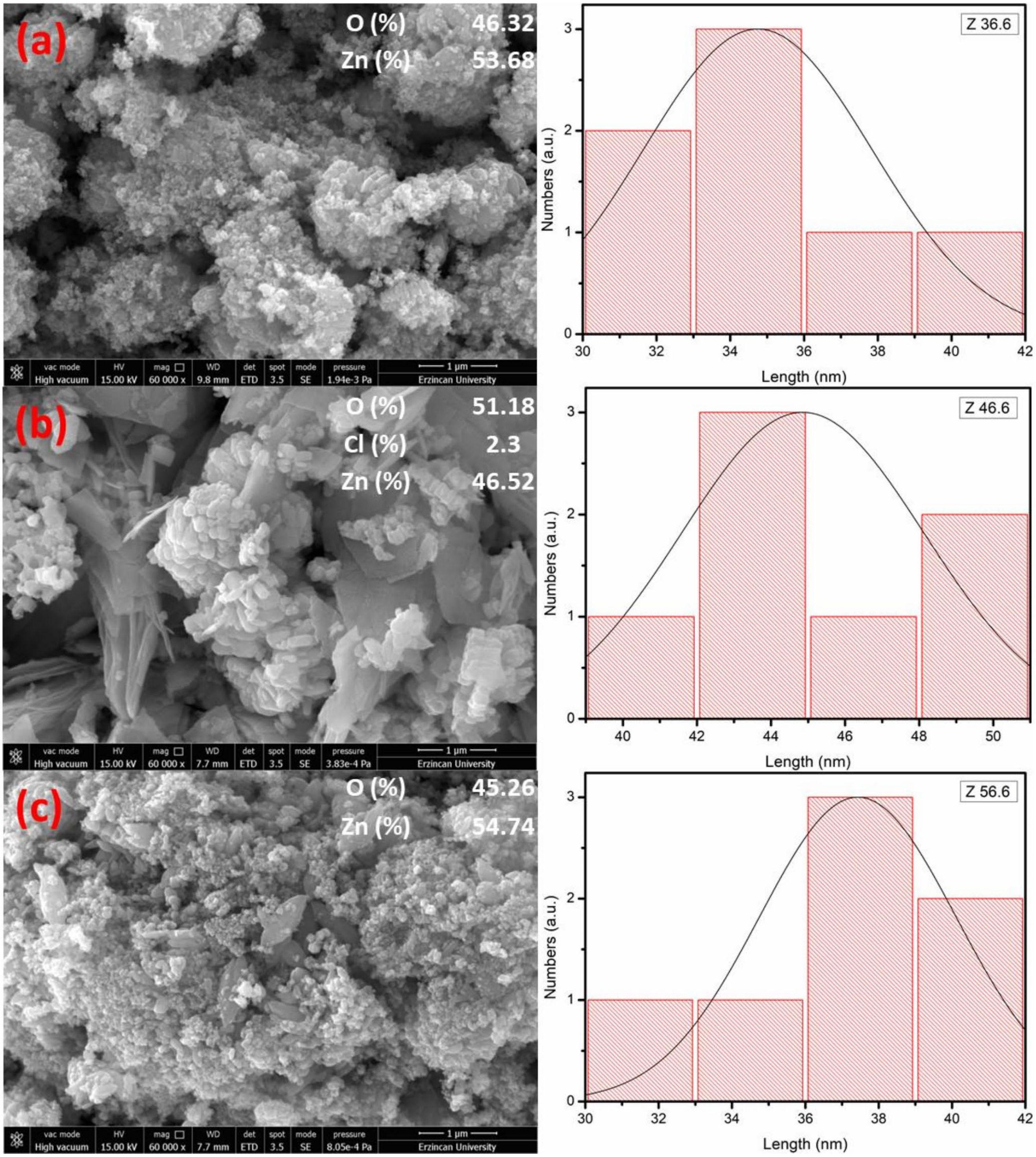

Fig. 4 SEM images of ZnO structures with histogram charts (**a**) Z 36.6 (**b**) Z 46.6 and (**c**) Z 56.6

to the effect of their surface dipoles, but have high growth rates due to the reduction in their surface energies. In the hydrothermal process, coordination or electrostatic interactions may facilitate the binding of the hydroxyl groups to the metal cations, as has been shown by Wang et al. [55]. This means that the absorbed Zn^{2+} ions react with OH^{-} groups to form $Zn(OH)_4{}^{2-}$. $Zn(OH)_4{}^{2-}$ is then dehydrated to form ZnO. Briefly, the concentration of OH^{-} in the reaction solution and thus the pH of the solution plays an important role in determining the morphology of the ZnO crystallites. The reason for using TEA in this study is due to the possibility of a selective attack on TEA molecules by surface ·OH radicals. Additionally, nanosized ZnO materials with a wide variety of shapes can be produced using TEA. Therefore, for the controlled synthesis of the flower-like ZnO morphology, the experimental parameters and in particular the pH of the solution (here 9) is an element to be optimized. The above discussion given above can be divided into reaction steps as shown in the study of Shi et al. [56].

$$Zn^{2+} + 2OH^{-} \rightarrow\ Zn\,(OH)_2 \tag{1}$$

$$Zn\,(OH)_2 + 2OH^{-} \rightarrow\ Zn\,(OH)_4^{2-} \tag{2}$$

$$Zn\,(OH)_4^{2-} \rightarrow\ ZnO + 2H_2O + 2OH^{-} \tag{3}$$

The average particle sizes for ZnO structures by histogram given in Fig. 4 were found to be 34.74 nm, 44.85 nm, and 37.42 nm, respectively. It is seen that these results are in agreement with the crystal size values calculated with different methods using the XRD data.

When the spectrum was examined, only the presence of Zn and O elements were detected. The data obtained as a result of the analysis show that no contamination was observed. The atomic percentages of the elements correspond to a 1:1 stoichiometry ratio. The atomic percentages of Zn and O elements can be seen in Fig. 4. The presence of Cl for Z 46.6 sample indicates an undesired impurity during the film synthesis stage.

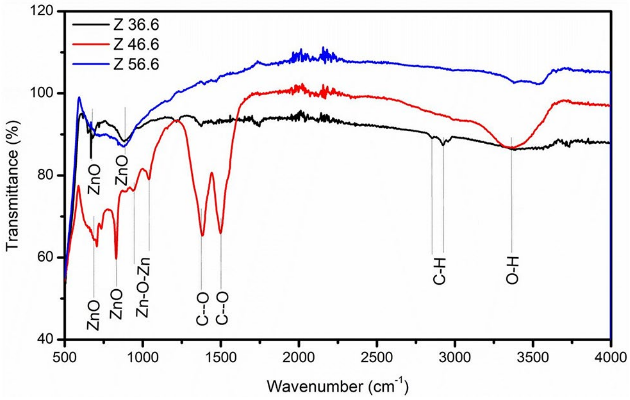

Fig. 5 FTIR spectra of ZnO structures

FTIR analysis

Fourier Transform Infrared Spectrophotometry (FTIR) is used to detect bond formations between elements in the structure to be measured. In this respect, the structural formation of the sample can be understood by measuring the vibration emitted by the bond formations within the structure at certain frequencies. This helps in the detection of functional groups in the measured material. It is possible to obtain spectral data in a wide spectrum range simultaneously with FTIR spectrometer devices. With this technique, it is possible to perform qualitative and quantitative analyzes of organic or inorganic solid, liquid and gas samples very quickly using IR active molecule properties.

In Fig. 5, there is a peak at the wave number value between 600 cm^{-1} and 850 cm^{-1} originating from Zn-O-Zn vibration. It is evident from the combined antisymmetric and symmetric stretching vibrations of Zn–O–Zn bond (945 cm^{-1}) and bending vibration (1041 cm^{-1}) [57]. The peak at wave number 1380 cm^{-1} and 1501 cm^{-1} corresponds to the C-O stretching mode [58]. OH stretching vibrations in the wave number range of 3200 to 3500 cm^{-1} arise from the presence of H_2O in the ZnO structure, and their intensity decreases and expands depending on the precursor concentration. Peaks appeared in the wave number range of 2856 and 2927 cm^{-1} due to symmetric and asymmetric C-H bonds. Metal oxides generally give absorption bands below 1000 cm^{-1} wave number due to interatomic vibrations. Changes in width, strength, and position with the addition of concentration of zinc precursor, particularly at 46.6 mM, may be the result of differences in growth chemistry or structural and atomic environment. The emergence of the absorption bands observed in the region and the increase in the C-O and C-H stretching frequencies that also occur at this precursor concentration are consistent with the change in the reaction kinetics between $ZnCl_2$ and [OH-] at the same concentration. The decrease in intensity at 56.6 mM concentration is probably due to the poor clearing stability of the instrument, or it can be concluded that the variation in peak intensities is due to the unequal presence of specific OH functional groups chemisorbed on the ZnO surfaces. In the literature, the absorption peak at a wave number of 453 cm^{-1} corresponds to the Zn-O stretching band in the ZnO lattice and is reported as the characteristic peak representing the ZnO structure [59].

Optical analysis

UV-Vis reflectance spectra of the samples as a function of the wavelength range from 200 to 500 nm are shown in Fig. 6. It is observed that all samples with different precursor amounts have two shoulder-shaped reflection bands in the UV region. The entrance of the precursors into ZnO lattice may be associated with the increase observed in the amount of reflectance and a further strong decrease for increasing precursor amount that was seen in the reflectance spectra. In addition, decrease in reflectance value after around 300 nm is linked to the optical transitions occurring in the optical band gap.

Another parameter to be considered in photocatalytic reactions is the band gap energy (Eg), because the photocatalyst needs radiation to be activated and the energy of this radiation depends on the Eg value of the semiconductor. The optical band gap of ZnO values were determined by the conversion of the reflectance values to absorbance. The Kubelka–Munk equation is used to convert the reflectance spectra to the equivalent of absorption spectra [60]:

$$F\left(R\right)=\frac{\left(1-R\right)^{2}}{2R}$$

F(R) and R are the equivalent of the absorption coefficient and the reflectivity, respectively. The $[(F(R)h\nu)]^2$- hν graph drawn to determine the E_g values of the ZnO structures is given in Fig. 7. These curves were extrapolated and the E_g values were calculated from the point where the linear parts intersect the x-axis.

Accordingly, the energy band values of the ZnO structures were found to be 3.38 eV, 3.42 eV, and 3.45 eV, respectively, with increasing $ZnCl_2$ amount. As can be seen here, as the precursor amount increases, the energy band gaps widen. This shows the effect of the blue shift obtained in the reflectance curve on the band gap. Also, in a study by Wang et al. [61], it was mentioned that as the concentration of oxygen vacancies increases, impurity states become more delocalized and overlap with the valence band edge, resulting in narrowing of the band gap. Considering the XRD and SEM results obtained in our results, in parallel with the observation made by Wang et al., the crystallite quality has increased as a function of $ZnCl_2$ doping, which means that the defects and impurity states on the surface are reduced. This may have caused an increase in the optical band gap. In addition, the presence of Cl^- ion in the structure was observed in the SEM analyses of sample Z 46.6, although the crystal quality showed a decreasing trend at Z 56.6. Due to this situation, as mentioned by Alshgari et al. [62], in their studies, a slight decrease was observed between the conduction band and valence band of ZnO due to the increased density of defects, and thus a higher optical band gap was observed in the Z 56.6 sample. Considering the data presented in Table 2 and the optical bandgap obtained with the photocatalytic performances of the samples synthesized in our study, it was observed that increasing $ZnCl_2$ concentration caused an increase in the optical bandgap, but led to a decrease in the photocatalytic reaction rate constants (k) and half-life values ($t_{1/2}$). These findings clearly confirm the

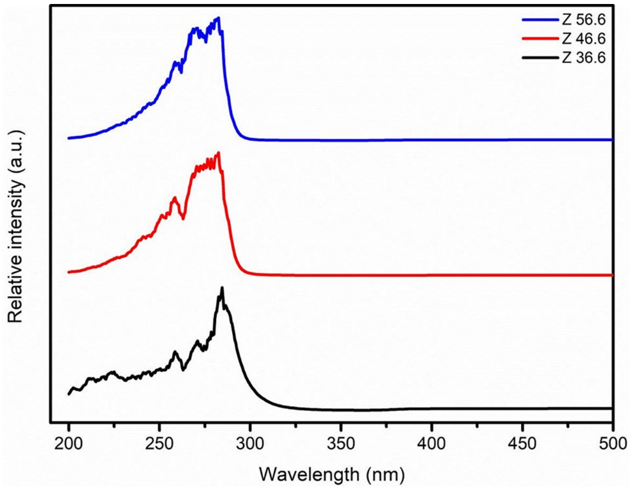

Fig. 6 Diffuse reflectance spectra of ZnO structures

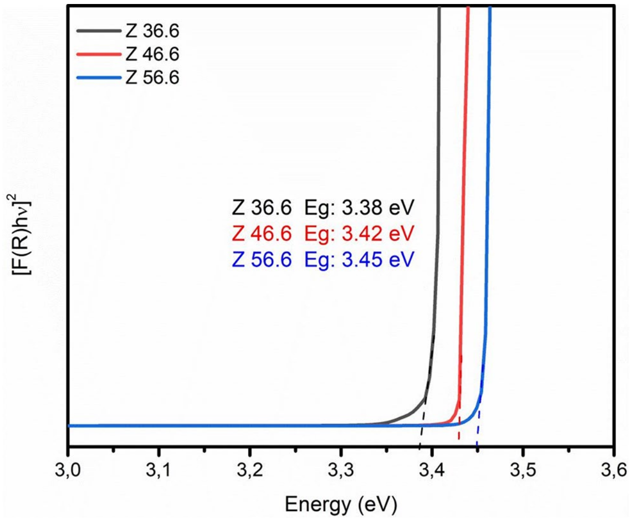

Fig. 7 $[(F(R)h\nu)]^2$- hν graph of ZnO structures

Table 2 Degradation reaction kinetic parameters of RhB + DR23 binary dyes using different precursor amounts

Kinetic Parameter		Z 36.6	Z 46.6	Z 56.6
k (1/min)	RhB	0.0218	0.0188	0.0131
	DR23	0.0150	0.0133	0.0187
R^2	RhB	0.6489	0.9800	0.8722
	DR23	0.5484	0.7386	0.7630
$t_{1/2}$ (min)	RhB	31.79	36.87	52.91
	DR23	46.21	52.11	37.06

inverse relationship between optical band gap and photocatalytic performance and demonstrate the consistency of the results of our study.

Photocatalytic analysis

Experiments were carried out in a closed UV-cabinet to determine the adsorption capacities and photocatalytic activities of the synthesized ZnO photocatalysts. The efficiency of the degradation of the binary mixtures of the dyes RhB and DR23, selected as pollutants, was studied simultaneously under the illumination of a UVA lamp with a wavelength of 365 nm in the UV chamber. The binary mixture was consisted of 22 ml of 5 ppm RhB and 28 ml of 30 ppm DR-23 dyes from RhB and DR-23 stock solutions, respectively, used to simulate impurity dyes. The solutions were placed in the dark for 30 min to ensure that all samples started at the same initial conditions to maintain consistency and reproducibility. The solutions were then transferred into tubes and kept in a UV cabinet under UVA light at varying time intervals.

Before measuring the absorbance values of the samples at the specified intervals on the UV-Vis spectrophotometer apparatus, the absorbance value was calibrated by zeroing it with RhB + DR23 dye solution. The tubes in which adsorption-desorption balance was achieved were first taken at the zeroth minute and the absorbance value was measured. This procedure was repeated for all samples under UVA light irradiation in the UV cabinet. Care was taken not to expose the tubes to light while taking them from the UV cabinet. The absorbance values obtained as a result of the 180-minute experimental measurement were noted. The changes in adsorption capacity and photocatalytic degradation efficiency percentages (%) of all samples depending on time (min) were examined. Dyes have specific characteristic absorption peaks in the visible region in the range of 400–700 nm. The photocatalytic activity in this process; it depends on the generation of electron-hole pairs in the band gap, which causes the formation of reactive radical species and species absorbed on the catalyst surface under UV light.

The percent color removal as a result of photocatalytic degradation was calculated with equation below:

$$color\ removal\ \% = \frac{C_0 - C_t}{C_0} x100$$

Here, C_0 is the initial dye concentration of the dye, and C_t is the dye concentration at any time t after the irradiation begins. The absorption spectra obtained as a result of the degradation of RhB + DR23 binary mixture dyestuffs solution with ZnO photocatalysts under the influence of UV light are given in Fig. 8. When Fig. 8 is examined, it is seen that the maximum absorption peaks for the binary mixture solution kept under UV light using ZnO structures as catalysts occur at a wavelength of 554 nm for RhB and 520 nm for DR23. Additionally, at the end of 180 min, Z 36.6, Z 46.6, and Z 56.6 synthesis provided color removal of 93.1% for RhB and 93.5% for DR23, 96.9% for RhB and 97.1% for DR23, and 94.3% for RhB and 93.5% for DR23, respectively. It was observed that the ZnO structure synthesized in the presence of 46.6 mM $ZnCl_2$ precursor concentration had the best photocatalytic activity in binary mixture dye removal. The fact that the degradation efficiency increases with increasing time intervals shows that the photocatalytic activity also increases. When the two dyes are combined into an integrated dye, it is expected to produce synergistic effects between the catalytic reactions, which can significantly accelerate the degradation of organic pollutants. The present study demonstrates the potential synergistic effect of ZnO structures in the catalytic process for the degradation of RhB and DR23 binary mixture dyes. The presence of $ZnCl_2$ precursors during photocatalysis causes faster degradation due to the provision of extra nuclei, which in turn creates additional deformations in the liquid medium, leading to the formation of more free radicals or additional oxidative species in the system, thus enhancing this effect.

The XRD results indicate that the sample prepared at 46.6 mM precursor concentration contains a chloride phase. These chloride ions may be present in the ZnO crystal lattice as impurities, such as interstitial and substitutional defects, and may have influenced the electronic structure of ZnO to enhance its photocatalytic performance. Additionally, the chloride phase may have contributed favorably to the active surface areas of the nanostructures by causing surface roughness. These speculations offer a potential explanation for why ZnO cauliflower nanostructures, obtained using 46.6 mM $ZnCl_2$ precursor salt, are responsible for the efficient photocatalytic degradation of both dyes. The increase in photocatalytic activity results with increasing time intervals was associated with efficient charge separation and improved absorption of light irradiation as a result of different precursor concentrations. Electrons activated by light rays falling on the ZnO structure react with oxygen molecules to form $O^{\bullet 2-}$ radicals. The positive holes in the valence band of ZnO can react with water to form OH^- radicals and positive protons. Positive holes enable the production of $OH^\bullet$ radicals from OH^- radicals. More OH^- radicals can be produced than $O^{\bullet 2-}$ radicals, which react with positive protons. Both $O^{\bullet 2-}$ and $OH^\bullet$ radicals are strong oxidizing agents that can degrade the binary mixture dye RhB + DR23 to CO_2 and H_2O, which are harmless to the environment and wastewater treatment applications [63].

The percentage degradation values of the ZnO synthesis, RhB + DR23 binary mixture dye, plotted against time in the

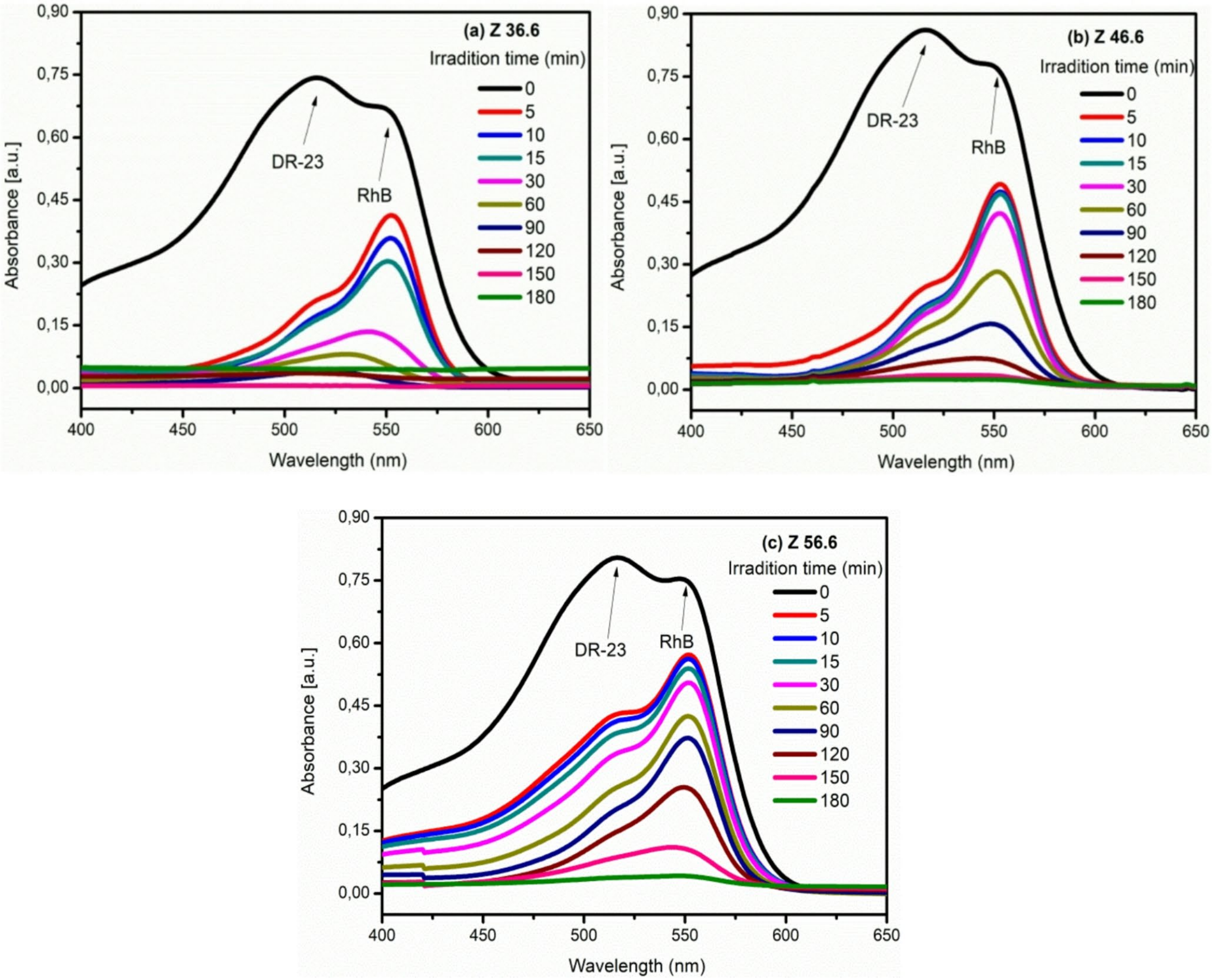

Fig. 8 Absorption spectra of ZnO photocatalysts under the influence of UV light

degradation curve under UV light are shown in Fig. 9. The photocatalytic activity of synthesized various morphologies of ZnO structures is presented in Table 3.

Photocatalytic degradation of RhB and DR23 dyes can be modeled by a first-order reaction. According to this model, the kinetic equation is as follows:

$$ln\left(\frac{C_t}{C_0}\right) = -kt$$

Here, C_0 is the dye concentration of the dye before the irradiation starts, and C_t is the dye concentration of the dye at time t after the irradiation starts, t is the reaction time and k is the reaction rate constant. The reaction rate constant k was calculated from the slope of the graph formed after drawing the graph of $\ln(C_t/C_0)$ against time. The first-order reaction kinetics graph of the photocatalytic degradation reaction of ZnO photocatalyst synthesized with different amounts of $ZnCl_2$ precursor and RhB + DR23 binary mixture dye is shown in Fig. 10.

In the kinetic model shown in Fig. 10, the slope of each line shows the reaction rate constant for that reaction. The kinetic parameters of the degradation reaction of RhB + DR23 binary mixture of dyes with ZnO photocatalyst synthesized in different amounts of $ZnCl_2$ are given in Table 2. In the extracted kinetic parameters, the highest R^2 value is the photocatalytic degradation reaction of RhB dye, which is degraded by the ZnO photocatalyst synthesized using 46.6 mM precursor concentration, but the reaction with the highest value of the reaction rate constant is the photocatalytic degradation reaction of 46.6 mM precursor concentration synthesis. As can be seen from the k and $t_{1/2}$ values, the synthesis with the best photocatalytic activity is the Z 36.6 synthesis. The electrons in the valence band can be excited to the conduction band and when the energy of the photons is greater than or equal to the band gap energy

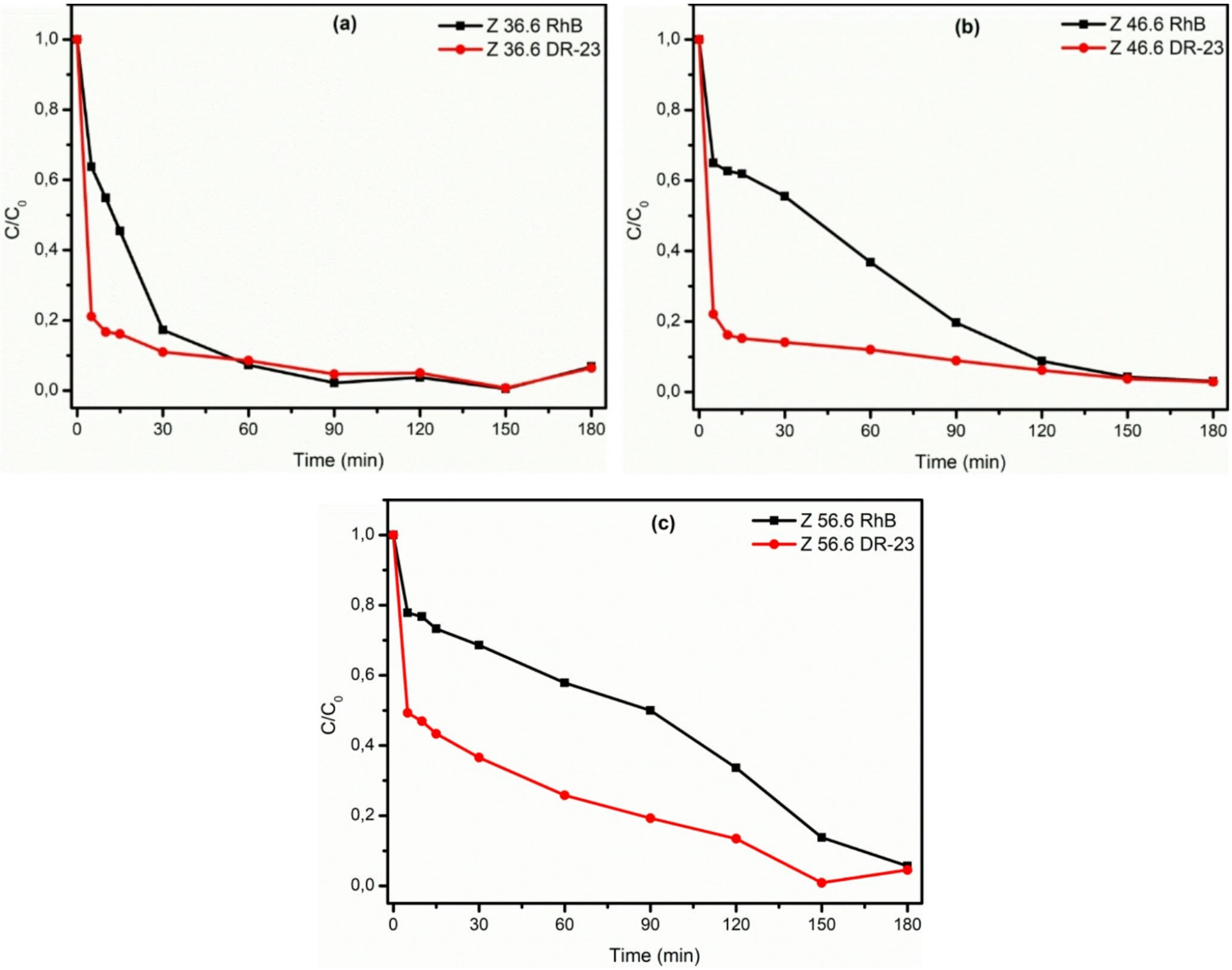

Fig. 9 Degradation graph of ZnO synthesis under UV light

Table 3 Comparison study of degradation for different morphological ZnO nanostructures

Photocatalyst	Pollutant	Degradation %	Irradiation time (min)	Refs.
ZnO/nanocellulose	MB	79	300	[64]
ZnO-Cube	RhB	71	240	[65]
ZnO	RhB	91	360	[66]
ZnO	RhB	93	240	[67]
Ba/ZnO	RhB	88.81	160	[68]
B/Sn doped ZnO nanoparticles	RhB	65.6	60	[69]
Fine pineapple leaf fiber/ZnO	Congo red	95	300	[70]
ZnO nanopowder	RhB	98.5	180	[71]

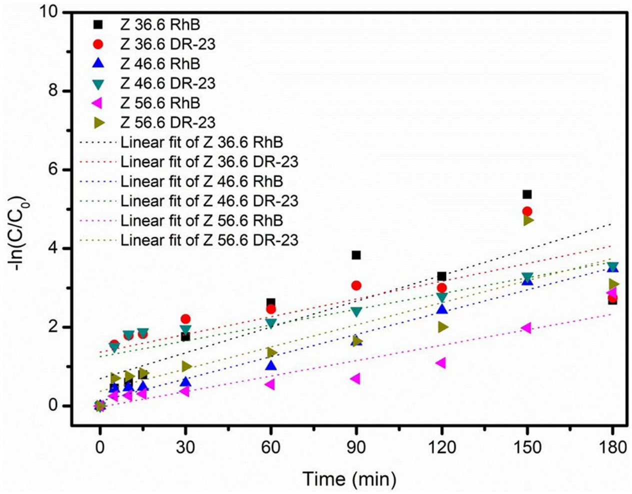

Fig. 10 Graph of kinetic model in the photocatalytic degradation of RhB + DR23 dye with the synthesized ZnO photocatalyst

of the ZnO films, electron-hole pairs are formed. These photoexcited electrons and holes interact with the binary dye mixture molecules and degrade the mixed dye through reactions. Thus, it is thought that at low precursor $ZnCl_2$

molarity in the ZnO structure, the photoexcited electrons act as effective trap sites, thus providing more degradation of the organic dye mixture and increasing its photocatalytic activity. In addition, in photocatalytic applications, the surface properties resulting from the lifetime of photoexcited holes and electrons are the main determinants of the photocatalytic activity of a structure. The crystal size of the Z 36.6 structure is lower than other structures. When both surface properties and crystal size analyses are considered, these properties can act as electron trapping centers while the holes can produce high levels of hydroxyl radicals and thus contribute to the degradation of organic dye molecules on the surface.

By determining the reaction rate constant k, the photocatalytic half-life ($t_{1/2}$) of the RhB + DR23 binary mixture of dyestuffs was calculated with equation given below:

$$t_{1/2} = \frac{ln2}{k}$$

The values of these data obtained from experimental studies of photocatalytic activity of photocatalysts in RhB + DR23 dyestuffs are shown in Table 2.

The photocatalytic activity of the ZnO structures in this study in the removal of RhB + DR23 binary mixture dyes was found to be high compared to studies conducted with other binary dyes given in Table 4. We believe that the reason for this is that the ZnO structures we produced have a wide direct band gap value and the defects in the band structure enable the recombination of electron-hole pairs to take longer. In addition, the fact that ZnO cauliflower structures have a small crystallite size and a porous morphology enables these materials to have high photocatalytic activity by increasing the active surface area, which is important for photocatalytic activity [72]. The most important parameter affecting photocatalytic activity is the lifetime of the photoexcited electrons and holes. According to the elemental analysis results, we think that the O element, which is less abundant in the structure of ZnOs than Zn, may have prevented the formation of these defects by settling in the surface volume regions, instead of creating defects in the material that can act as junction centers for electrons and holes in the structure. In this way, the recombination of electron and hole pairs in the photocatalysis process may have been prolonged and the photocatalytic activity may have increased [73].

Table 4 Comparison of the photocatalytic performance of different binary dyes mixture

Photocatalyst	Mixture of dyes	Degradation %	Irradiation time (min)	Refs.
Cu_2SnS_3 nanostructures	RhB + MO	80	240	[74]
UiO-66/$BiFeO_3$	RhB + MO	> 82 and > 84	180	[75]
ZnS Quantum Dots	RhB + BG	> 88 and > 72	-	[76]
TiO_2 nanoparticles	RhB + MB	> 92 and > 93	180	[77]
$CeO_2/Co_3O_4/Ag/Ag_3PO_4$	RhB + MB	> 63	100	[78]
Chitosan/CuO/CeO_2	MB + AB113	92 and 91	60	[79]
ZnO	RhB + DR23	94 and 95	180	This work

As can be seen, the Z 46.6 photocatalyst showed good activity in degrading all the dyes, but the time required for complete degradation of each dye varied. The different sensitivity of the dyes to photocatalytic degradation by Z 46.6 was attributed to the nature of the dyes, their molecular structures and different reactivity during the photocatalysis process, dye concentration, absorption characteristics and alignment of the energy levels of the dyes with the energy levels of the coumarin-sensitive ZnO photocatalysts [80]. Furthermore, depending on the nature of the dyes, pH conditions can have a significant effect on the degradation efficiency, as some dyes degrade faster at moderate pH ranges while others have better degradation pathways at strongly basic or acidic pH [81]. Similar study was conducted by Cherif et al., the ZnO thin films prepared by spray pyrolysis showed a photocatalytic performance of 73% and 61% depending on the different conditions [82].

Figure 11 shows the photocurrent as a function of time results of the structures that provide us with information about the charge recombination processes taking place in the materials investigated in this work. As seen in the figure, when the light is turned on, the current suddenly increases and reaches a constant value depending on the light intensity. When the light is turned off, the current reaches its initial value. These results show that the fabricated diodes exhibit strong photosensitive behavior. When the diode is exposed to light intensity, the amount of charge carriers created by the light increases and then current is generated due to the presence of free electrons. During synthesis, due to the creation of crystal lattice distortion, electron/hole recombination was greatly reduced. In addition, the test of intermittent on-off visible light cycle used to test the light sensitivity of photocatalytic activity also shows a noble response. Furthermore, the high photoresponse indicates excellent separation of photogenerated charge carriers. The photocurrents of the Z 46.6 and Z 56.6 structures are significantly higher than that of the Z 36.6 structure under light-on and light-off conditions, implying low electron-hole recombination rate and excellent electron transport for

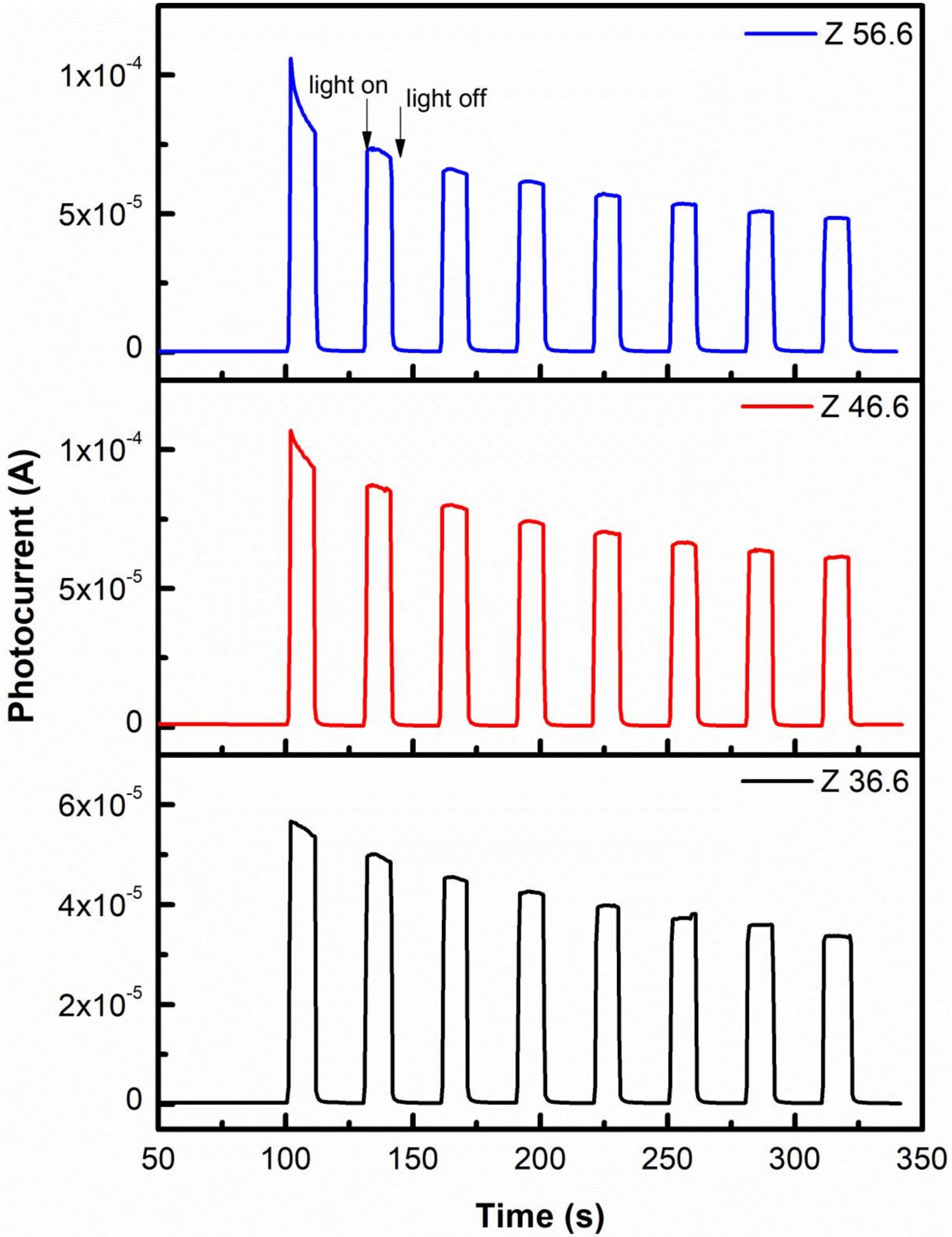

Fig. 11 Current transient measurements of ZnO structures

these structures. Although the photocurrent measurements show differences in the carrier decomposition efficiency of the samples, these results do not fully reflect all aspects of photocatalytic performance. Not only the carrier decomposition efficiency, but also surface defects, light absorption capacity and surface reaction kinetics all have a combined effect on photocatalytic processes [83]. In this context, the poor crystallite quality of sample Z 36.6 compared to the other samples led to a high level of defects, which can be considered as energy levels that can function as reaction centers and accelerate redox reactions on the surface, and thus more reactive oxygen species were produced on the surface. At the same time, considering the energy level of the light used, it can be concluded that the Z 36.6 sample can form more electron-vacancy pairs. In conclusion, based on the results of the Z 36.6 sample, it is thought that the photocatalytic performance of the Z 36.6 sample is higher than the others, despite the lower photocurrent values, due to the more efficient light absorption and the contribution of the surface-active sites to the reaction kinetics.

Conclusion

In this study, ZnO structures, a material that attracts attention in photocatalytic applications, were produced by hydrothermal synthesis method with different precursor concentrations and their potential for use in these areas was investigated. To determine the usability of ZnO structures in these areas, their structural, optical and photocatalytic properties were examined in detail using appropriate analysis techniques. As a result of examining the structural properties of ZnO, it was determined that the crystal structure was formed by hexagonal wurtzite structure and the crystallization level was high. It was determined that the dominant growth was especially in the (100), (002) and (101) directions. In addition, it was found that the average crystal size had crystallization of different sizes in different directions of growth and that the crystal sizes forming the crystal structure in these directions were between 27–40 nm. Surface properties and elemental analyzes of ZnO structures were performed with SEM and EDS. As a result of examining the SEM images obtained at different magnifications, it was determined that the morphological structure of ZnO structures produced by the hydrothermal synthesis method had "cauliflower" type morphology of large and small sizes. Elemental analysis results showed that there was not much difference between the atomic percentages of Zn and O. This shows that ZnO structures have an almost stoichiometric structure. The optical study suggests that the optical band gap of ZnO can be tuned according to the precursor amount to alter its properties beneficial for photocatalysis. The photocatalytic activity of ZnO structures was determined by performing photocatalytic tests for RhB + DR23 binary mixture of dyestuffs. It was determined that the amount of $ZnCl_2$ precursor in the synthesis stage affected the resulting product and photocatalytic activity. As a result of tests performed with dyes, it was determined that ZnO photocatalysts have high degradability in short irradiation times. In addition, the photocatalytic activity rate constant and percent degradation values, which determine the photocatalytic activity, were calculated with first-order rate equations by examining the photocatalytic activity kinetics. As a result of these calculations, it was determined that ZnO structures had a high rate constant and reached 97% degradation value in a short time. Moreover, different amount of precursor increased the photocatalytic efficiency for ZnO structures because it decreases the recombination and separation efficiency of electron-hole pair. As a result, in this study, it was determined that ZnO structures produced with a practical and low-cost production technique have high photocatalytic properties and have potential for use in these areas.

Author contributions EE: Methodology, writing—original draft, data curation, visualization. BBC: writing-original draft, data curation, investigation, validation. ME and MY: writing-review and editing, conceptualization.

Funding Open access funding provided by the Scientific and Technological Research Council of Türkiye (TÜBİTAK).
The authors declare that no funds, grants, or other support were received during the preparation of this manuscript.

Data availability Data available on request from the authors.

Declarations

Competing interests The authors declare no competing interests.

References

1. Nawaz, S., Rashid, E.U., Bagheri, A.R., Aramesh, N., Bhatt, P., Ali, N., Nguyen, T.A., Bilal, M.: Mitigation of environmentally hazardous pollutants by magnetically responsive composite materials. Chemosphere. **276**, 130241 (2021)

2. Farhan, A., Rashid, E.U., Waqas, M., Ahmad, H., Nawaz, S., Munawar, J., Rahdar, A., Varjani, S., Bilal, M.: Graphene-based nanocomposites and nanohybrids for the abatement of agro-industrial pollutants in aqueous environments. Environ. Pollut. **308**, 119557 (2022)
3. Lu, S., Zhu, K., Hayat, T., Alharbi, N.S., Chen, C., Song, G., Chen, D., Sun, Y.: Influence of carbonate on sequestration of U (VI) on perovskite. J. Hazard. Mater. **364**, 100–107 (2019)
4. Seliem, M.K., El-Mahrouk, M.E., El-Banna, A.N., Hafez, Y.M., Dewir, Y.H.: Micropropagation of Philodendron selloum: Influence of copper sulfate on endophytic bacterial contamination, antioxidant enzyme activity, electrolyte leakage, and plant survival. S Afr. J. Bot. **139**, 230–240 (2021)
5. Al-Khthami, N.D., Altalhi, T., Alsawat, M., Amin, M.S., Alghamdi, Y.G., Zaki, Z.I., Mohamed, R.M.: $FeYO_3$@rGO nanocomposites: Synthesis, characterization and application in photooxidative degradation of atrazine under visible light. Mater. Express. **11**(5), 706–716 (2021)
6. Ernawati, L., et al.: Experimental data of $CaTiO_3$ photocatalyst for degradation of organic pollutants (brilliant green dye)–Green synthesis, characterization and kinetic study. Data Br. **32**, 106099 (2020)
7. Alrobei, H., et al.: Adsorption of anionic dye on eco-friendly synthesised reduced graphene oxide anchored with lanthanum aluminate: Isotherms, kinetics and statistical error analysis. Ceram. Int. **47**(7), 10322–10331 (2021)
8. Bagherzadeh, S.B., Kazemeini, M., Mahmoodi, N.M.: A study of the DR23 dye photocatalytic degradation utilizing a magnetic hybrid nanocomposite of MIL-53 (Fe)/$CoFe_2O_4$: Facile synthesis and kinetic investigations. J. Mol. Liq. **301**, 112427 (2020)
9. Ali, S.M., Eskandrani, A.A.: The sorption performance of cetyl trimethyl ammonium bromide-capped $La_{0.9}Sr_{0.1}FeO_3$ perovskite for organic pollutants from industrial processes. Molecules. **25**(7), 1640 (2020)
10. Garba, Z.N., Xiao, W., Zhou, W., Lawan, I., Jiang, Y., Zhang, M., Yuan, Z.: Process optimization and synthesis of lanthanum-cobalt perovskite type nanoparticles ($LaCoO_3$) prepared by modified proteic method: Application of response surface methodology. Korean J. Chem. Eng. **36**, 1826–1838 (2019)
11. Bresolin, B.M., Hammouda, S.B., Sillanpää, M.: Methylammonium Iodo bismuthate perovskite $(CH_3NH_3)_3Bi_2I_9$ as new effective visible light-responsive photocatalyst for degradation of environment pollutants. J. Photochem. Photobiol A. **376**, 116–126 (2019)
12. Reyes-Pérez, F., Gallardo, J.J., Aguilar, T., Alcántara, R., Fernández-Lorenzo, C., Navas, J.: Visible-light-enhanced photocatalytic activity of totally inorganic halide-based perovskite. ChemistrySelect. **3**(36), 10226–10235 (2018)
13. Kotp, Y.H.: Removal of organic pollutants using polysulfone ultrafiltration membrane containing polystyrene silicomolybdate nanoparticles: Case study: Borg El Arab area. J. Water Process. Eng. **30**, 100553 (2019)
14. Crini, G., Lichtfouse, E.: Advantages and disadvantages of techniques used for wastewater treatment. Environ. Chem. Lett. **17**, 145–155 (2019)
15. Zazou, H., et al.: Treatment of textile industry wastewater by electrocoagulation coupled with electrochemical advanced oxidation process. J. Water Process. Eng. **28**, 214–221 (2019)
16. Muthukumar, G., Arjunkumar, B., Vignesh, R., Ramalingam, G., Prashant, K.: A study of Photocatalytic Degradation of Betalain Pigment from Kitchen Waste, Semiconductive Nanostructured TiO_2 used as a Photocatalyst. Mater. Sci. Res. India **15**(3), (2018)
17. Zhong, Y., et al.: Graphene oxide modified membrane for highly efficient wastewater treatment by dynamic combination of nanofiltration and catalysis. J. Hazard. Mater. **397**, 122774 (2020)
18. Wang, K., Guan, Z., He, Y., Fan, M.: Harnessing Zinc Stannate for Sustainable Energy and Environment Solutions: Advances in Photocatalytic, Piezocatalytic, and Piezo-Photocatalytic technologies. Nano Energy. **133**, 110518 (2024)
19. Wang, K., He, Y.: Recent advances in metal titanate-based piezocatalysts: Enhancing catalytic performance through improved piezoelectric properties and regulated carrier transport. Chin. J. Catal. **61**, 111–134 (2024)
20. Huang, X., Zhang, K., Peng, B., Wang, G., Muhler, M., Wang, F.: Ceria-based materials for thermocatalytic and photocatalytic organic synthesis. ACS Catal. **11**(15), 9618–9678 (2021)
21. Kumar, A., Thakur, P.R., Sharma, G., Naushad, M., Rana, A., Mola, G.T., Stadler, F.J.: Carbon Nitride, metal nitrides, phosphides, chalcogenides, perovskites and carbides nanophotocatalysts for environmental applications. Environ. Chem. Lett. **17**, 655–682 (2019)
22. Humayun, M., Wang, C., Luo, W.: Recent progress in the synthesis and applications of composite photocatalysts: A critical review. Small Methods. **6**(2), 2101395 (2022)
23. Alam, M.W., et al.: Novel copper-zinc-manganese ternary metal oxide nanocomposite as heterogeneous catalyst for glucose sensor and antibacterial activity. Antioxidants. **11**(6), 1064 (2022)
24. Raja, A., et al.: Eco-friendly preparation of zinc oxide nanoparticles using Tabernaemontana divaricata and its photocatalytic and antimicrobial activity. J. Photochem. Photobiol B: Biol. **181**, 53–58 (2018)
25. Hitam, C.N., Jalil, A.A.: A review on exploration of Fe_2O_3 photocatalyst towards degradation of dyes and organic contaminants. J. Environ. Manag. **258**, 110050 (2020)
26. Ali, M.M., Haque, M.J., Kabir, M.H., Kaiyum, M.A., Rahman, M.S.: Nano synthesis of ZnO–TiO_2 composites by sol-gel method and evaluation of their antibacterial, optical and photocatalytic activities. Results Mater. **11**, 100199 (2021)
27. Gao, X., Li, L., An, M., Zheng, T., Ma, F.: ZnO QDs and three-dimensional ordered macroporous structure synergistically enhance the photocatalytic degradation and hydrogen evolution performance of WO_3/TiO_2 composites. J. Phys. Chem. Solids. **165**, 110655 (2022)
28. Malik, M., et al.: Engineering of a hybrid g-C_3N_4/ZnO-W/Co_x heterojunction photocatalyst for the removal of methylene blue dye. Catalysts. **13**(5), 813 (2023)
29. Singh, D., et al.: Photodegradation of Methylene blue and rhodamine B using potato starch mediated zinc oxide nanoparticles and its calcium nanocomposites: Greener approach. Appl. Chem. Eng. **6**(1), 94–103 (2023)
30. He, W., Zhao, H., Jia, H., Yin, J.J., Zheng, Z.: Determination of reactive oxygen species from ZnO micro-nano structures with shape-dependent photocatalytic activity. Mater. Res. Bull. **53**, 246–250 (2014)
31. Chen, Y., Zhao, H., Liu, B., Yang, H.: Charge separation between wurtzite ZnO polar {001} surfaces and their enhanced photocatalytic activity. Appl. Catal. B: Environ. **163**, 189–197 (2015)
32. Teixeira, I.F., Barbosa, E.C., Tsang, S.C.E., Camargo, P.H.: Carbon nitrides and metal nanoparticles: From controlled synthesis to design principles for improved photocatalysis. Chem. Soc. Rev. **47**(20), 7783–7817 (2018)
33. Arun, V., Prabhu, S., Priyadharsan, A., Maadeswaran, P., Sohila, S., Ramesh, R., Kumar, A.S.: Facile, low cost synthesis of cauliflower-shaped ZnO with MWCNT/rGO nanocomposites and their photocatalytic activity. J. Mater. Sci: Mater. Electron. **32**, 15763–15777 (2021)
34. Hassanein, A., Salahuddin, N., Matsuda, A., Kawamura, G., Elfiky, M.: Fabrication of biosensor based on Chitosan-ZnO/Polypyrrole nanocomposite modified carbon paste electrode for electroanalytical application. Mater. Sci. Eng. C. **80**, 494–501 (2017)

35. Liu, X., et al.: Porous cauliflower-like molybdenum disulfide/cadmium sulfide hybrid micro/nano structure: Enhanced visible light absorption ability and photocatalytic activity. J. Colloid Interface Sci. **590**, 352–364 (2021)
36. Bandeira, M., Giovanela, M., Roesch-Ely, M., Devine, D.M., da Silva Crespo, J.: Green synthesis of zinc oxide nanoparticles: A review of the synthesis methodology and mechanism of formation. Sustain. Chem. Pharm. **15**, 100223 (2020)
37. Haque, M.J., Bellah, M.M., Hassan, M.R., Rahman, S.: Synthesis of ZnO nanoparticles by two different methods & comparison of their structural, antibacterial, photocatalytic and optical properties. Nano Express. **1**(1), 010007 (2020)
38. Zhang, C., Ren, X., Wang, K., Liang, X., Wu, Y., He, Y.: Boosting piezocatalytic efficiency: Thin carbon layer-modified ZnO for superior rhodamine B degradation. Ceram. Int. **50**(21), 43340–43344 (2024)
39. Chu, Y., Zhao, C., Zheng, Y., Ren, X., Yuan, S., Zhao, L.,… He, Y.: ZnSnO3-derived ZnSnO3/ZIF-8 composites with enhanced adsorption and photocatalytic activity in RhB degradation and CO2 reduction. J. Environ. Sci. 2024.
40. Ren, X., Chu, Y., Yuan, S., Zheng, Y., Zeng, Z., Xia, C.,… He, Y.: Enhanced piezocatalytic RhB degradation with ZnSnO3 Nanocube-modified Bi4Ti3O12 composite catalyst by harnessing ultrasonic energy. J. Environ. Manage. **370**, 122776 (2024).
41. Baruah, S., Dutta, J.: Zinc stannate nanostructures: Hydrothermal synthesis. Sci. Technol. Adv. Mater. **12**(1), 013004 (2011)
42. Khaghanpour, Z., Naghibi, S.: Perforated ZnO nanoflakes as a new feature of ZnO achieved by the hydrothermal-assisted sol–gel technique. J. Nanostructure Chem. **7**(1), 55–59 (2017)
43. Chatzigoulas, A., Karathanou, K., Dellis, D., Cournia, Z.: NanoCrystal: A web-based crystallographic tool for the construction of nanoparticles based on their crystal habit. J. Chem. Inf. Model. **58**(12), 2380–2386 (2018)
44. Kumar, S., Arora, D., Dhupar, A., Sharma, V., Sharma, J.K., Sharma, S.K., Gaur, A.: Structural and optical properties of polycrystalline ZnO nanopowder synthesized by direct precipitation technique. J. Nano- Electron. Phys. **12**(4), 04027 (2020)
45. Mrad, M., Chouchene, B., Chaabane, T.B.: Effects of zinc precursor, basicity and temperature on the aqueous synthesis of ZnO nanocrystals. S Afr. J. Chem. **71**, 103–110 (2018)
46. Emel, O., Tuncolu, İ.G., Aciksari, C., Suvaci, E.: Effect of precursor type on zinc oxide formation and morphology development during hydrothermal synthesis. Hittite j. sci. eng. **3**(2), 73–80 (2016)
47. Bouderbala, I.Y., Guessoum, A., Rabhi, S., Bouhlassa, O., Bouras, I.E.: Optical band-diagram, Urbach energy tails associated with photoluminescence emission in defected ZnO thin films deposited by sol–gel process dip-coating: Effect of precursor concentration. Appl. Phys. A. **130**(3), 205 (2024)
48. Erdoğan, E., Turgut, G., Yilmaz, M.: Sol–gel spin coating derived cadmium oxide semiconductor thin films: Effect of lutetium contribution. Optik. **240**, 166819 (2021)
49. Erdoğan, E., Yilmaz, M., Aydogan, S., Turgut, G.: Investigation of neodymium rare earth element doping in spray-coated zinc oxide thin films. J. Mater. Sci: Mater. Electron. **32**, 1379–1391 (2021)
50. Basnet, P., Chatterjee, S.: Structure-directing property and growth mechanism induced by capping agents in nanostructured ZnO during hydrothermal synthesis—A systematic review. Nano-Struct Nano-Objects. **22**, 100426 (2020)
51. Wu, K.J., Edmund, C.M., Shang, C., Guo, Z.: Nucleation and growth in solution synthesis of nanostructures–from fundamentals to advanced applications. Prog Mater. Sci. **123**, 100821 (2022)
52. Mustapha, S., et al.: Comparative study of crystallite size using Williamson-Hall and Debye-Scherrer plots for ZnO nanoparticles. Adv. Nat. Sci: Nanosci. Nanotechnol. **10**(4), 045013 (2019)
53. Rajamanickam, S., Mohammad, S.M., Hassan, Z.: Effect of zinc acetate dihydrate concentration on morphology of ZnO seed layer and ZnO nanorods grown by hydrothermal method. Colloid Interface Sci. Commun. **38**, 1–13 (2020)
54. Feng, J.J., Liao, Q.C., Wang, A.J., Chen, J.R.: Mannite supported hydrothermal synthesis of hollow flower-like ZnO structures for photocatalytic applications. CrystEngComm. **13**(12), 4202–4210 (2011)
55. Wang, A.J., Liao, Q.C., Feng, J.J., Zhang, P.P., Li, A.Q., Wang, J.J.: Apple pectin-mediated green synthesis of hollow double-caged peanut-like ZnO hierarchical superstructures and photocatalytic applications. CrystEngComm. **14**(1), 256–263 (2012)
56. Shi, R., Yang, P., Wang, J., Zhang, A., Zhu, Y., Cao, Y., Ma, Q.: Growth of flower-like ZnO via surfactant-free hydrothermal synthesis on ITO substrate at low temperature. CrystEngComm. **14**(18), 5996–6003 (2012)
57. Jafari, A., Ghane, M., Arastoo, S.H.: Synergistic antibacterial effects of nano zinc oxide combined with silver nanocrystals. Afr. J. Microbiol. Res. **5**(30), 5465–5473 (2011)
58. Srivastava, A., Kumar, N., Misra, K.P., Khare, S.: Blue-light luminescence enhancement and increased band gap from calcium-doped zinc oxide nanoparticle films. Mater. Sci. Semicond. Process. **26**, 259–266 (2014)
59. Sohail, A., Faraz, M., Arif, H., Bhat, S.A., Siddiqui, A.A., Bano, B.: Deciphering the interaction of bovine heart cystatin with ZnO nanoparticles: Spectroscopic and thermodynamic approach. Int. J. Biol. Macromol. **95**, 1056–1063 (2017)
60. Ansari, N., Kavish, M., Wagay, J.A., Khan, Z., Khan, A.R., Ahmed, S., Rahman, Q.I.: Sustainable synthesis of ZnO nanostructures using Ficus religiosa leaf extract with enhanced photocatalytic and antibacterial activity. Mater. Sci. Eng. B. **310**, 117752 (2024)
61. Wang, J., Wang, Z., Huang, B., Ma, Y., Liu, Y., Qin, X., Zhang, X., Dai, Y.: Oxygen vacancy induced band-gap narrowing and enhanced visible light photocatalytic activity of ZnO. ACS Appl. Mater. Interfaces. **4**(8), 4024–4030 (2012)
62. Alshgari, R. A., Ujjan, Z. A., Shah, A. A., Bhatti, M. A., Tahira, A., Shaikh, N.M.,… Ibhupoto, Z. H.: ZnO nanostructures doped with various chloride ion concentrations for efficient photocatalytic degradation of methylene blue in alkaline and acidic media. Molecules. **27**(24), 8726 (2022).
63. Li, H., Liu, J., Wang, C., Yang, H., Xue, X.: Oxygen vacancies-enriched and porous hierarchical structures of ZnO microspheres with improved photocatalytic performance. Vacuum. **199**, 110891 (2022)
64. Lefatshe, K., Muiva, C.M., Kebaabetswe, L.P.: Extraction of nanocellulose and in-situ casting of ZnO/cellulose nanocomposite with enhanced photocatalytic and antibacterial activity. Carbohydr. Polym. **164**, 301–318 (2017)
65. Al-Bedairy, M.A., Alshamsi, H.A.H.: Environmentally friendly preparation of zinc oxide, study catalytic performance of photodegradation by sunlight for rhodamine B dye. Eurasian J. Anal. Chem. **13**(6), 1–9 (2018)
66. Yudasari, N., Kennedy, D.S., Suliyanti, M.M.: Pulse laser deposition (PLD) technique for ZnO photocatalyst fabrication. J. Phys. Conf. Ser. **1191**, 012009 (2019)
67. Kaviyarasu, K., et al.: Elucidation of photocatalysis, photoluminescence and antibacterial studies of ZnO thin films by spin coating method. J. Photochem. Photobiol B: Biol. **173**, 466–475 (2017)
68. Shirdel, B., Behnajady, M.A.: Visible-light-induced degradation of rhodamine B by Ba doped ZnO nanoparticles. J. Mol. Liq. **315**, 113633 (2020)

69. Ahmed, A.Z., Islam, M.M., Islam, M.M.U., Masum, S.M., Islam, R., Molla, M.A.I.: Fabrication and characterization of B/Sn-doped ZnO nanoparticles via mechanochemical method for photocatalytic degradation of rhodamine B. Inorg. Nano-Met. **51**(10), 1369–1378 (2020)
70. Deebansok, S., Amornsakchai, T., Sae-Ear, P., Siriphannon, P., Smith, S.M.: Sphere-like and flake-like ZnO immobilized on pineapple leaf fibers as easy-to-recover photocatalyst for the degradation of Congo red. J. Environ. Chem. Eng. **9**(2), 104746 (2021)
71. Erdogan, E., Eden, C., Canpolat, N., Cirak, C., Yilmaz, M.: Optimizing the structural and photocatalytic performance of Ag-decorated ZnO/Zn(OH)$_2$ nanoparticles for RhB degradation. Int. J. Appl. Ceram. **21**, 2010–2023 (2024)
72. Wang, S., Kuang, P., Cheng, B., Yu, J., Jiang, C.: ZnO hierarchical microsphere for enhanced photocatalytic activity. J. Alloys Compd. **741**, 622–632 (2018)
73. Chang, Y., Xu, J., Zhang, Y., Ma, S., Xin, L., Zhu, L., Xu, C.: Optical properties and photocatalytic performances of pd modified ZnO samples. J. Phys. Chem. C. **113**(43), 18761–18767 (2009)
74. Zaman, M.B., Poolla, R.: Morphological tuning of hydrothermally derived visible light active Cu$_2$SnS$_3$ nanostructures and their applications in photocatalytic degradation of reactive industrial dyes. Opt. Mater. **104**, 109853 (2020)
75. Bargozideh, S., Tasviri, M., Shekarabi, S., Daneshgar, H.: Magnetic BiFeO$_3$ decorated UiO-66 as ap–n heterojunction photocatalyst for simultaneous degradation of a binary mixture of anionic and cationic dyes. New. J. Chem. **44**(30), 13083–13092 (2020)
76. Ajibade, P.A., Oluwalana, A.E.: Photocatalytic degradation of single and binary mixture of brilliant green and rhodamine B dyes by zinc sulfide quantum dots. Molecules. **26**(24), 7686 (2021)
77. Suhaimi, N.A.A., et al.: Domination of methylene blue over rhodamine B during simultaneous photocatalytic degradation by TiO$_2$ nanoparticles in an aqueous binary solution under UV irradiation. React. Kinet Mech. Catal. **135**, 511–527 (2022)
78. Sabzehmeidani, M.M., Karimi, H., Ghaedi, M.: Degradation of binary mixtures of dyes by step-scheme quaternary photocatalyst in continuous flow-loop ultrasound assisted micro-photoreactor. J. Mol. Liq. **388**, 122830 (2023)
79. Nisha, U.M., Venkatesh, D., Arulmurugan, S., Kistan, A., Rajeswaran, P., Karthik, P.S.: Assessment of solar light sensitive Chitosan integrated CeO$_2$-CuO ternary composites for the efficient degradation of Malachite Green, Acid Blue 113 dyes and microbial studies. Inorg. Chem. Commun. **160**, 111942 (2024)
80. Verma, S., Rao, B.T., Jayabalan, J., Rai, S.K., Phase, D.M., Srivastava, A.K., Kaul, R.: Studies on growth of au cube-ZnO core-shell nanoparticles for photocatalytic degradation of methylene blue and methyl orange dyes in aqueous media and in presence of different scavengers. J. Environ. Chem. Eng. **7**(4), 103209 (2019)
81. Verma, S., Rao, B.T., Singh, R., Kaul, R.: Photocatalytic degradation kinetics of cationic and anionic dyes using Au–ZnO nanorods: Role of pH for selective and simultaneous degradation of binary dye mixtures. Ceram. Int. **47**(24), 34751–34764 (2021)
82. Cherif, S., et al.: The photocatalytic degradation of a binary textile dyes mixture within a new configuration of loop reactor using ZnO thin film-phytotoxicity control. Comptes Rendus Chim. **25**(S3), 1–19 (2022)
83. Wang, J., Xia, Y., Dong, Y., Chen, R., Xiang, L., Komarneni, S.: Defect-rich ZnO nanosheets of high surface area as an efficient visible-light photocatalyst. Appl. Catal. B: Environ. **192**, 8–16 (2016)